JOURNAL OF GEOPHYSICAL RESEARCH, VOL. 113, D09205, doi:10.1029/2007JD009237, 2008

Characterization of the atmosphere during SEN2FLEX 2005 field campaign

Víctor Estellés,[1] Francisco Molero,[2] José L. Gómez-Amo,[1] Juan C. Fortea,[3] Roberto Pedrós,[1] María P. Utrillas,[1] Manuel Pujadas,[2] Luis Guanter,[4] and José A. Martínez-Lozano[1]

Received 30 July 2007; revised 23 November 2007; accepted 28 January 2008; published 14 May 2008.

[1] The European Space Agency carried out the Sentinel-2 and Fluorescence Experiment (SEN2FLEX) campaign in Barrax (Spain) during the summer of 2005, with the main objective of observe solar induced fluorescence signal using the AirFLEX airborne instrument over different vegetation targets in order to verify signal suitability for observations from space as proposed in the FLEX mission. A highly precise atmospheric correction is mandatory for adequate measurements of the AirFLEX instrument; thus a complete characterization of the atmosphere was programmed in SEN2FLEX in order to document the presence of atmospheric aerosols above the experimental area, as their effects represent the major source of uncertainty in atmospheric correction algorithms. In this work, an analysis of the atmospheric data is presented focusing on its eventual application to atmospheric correction of satellite imagery. Validation of Compact Airborne Spectrographic Imager (CASI) aerosol optical depth and columnar water vapor content retrievals has been included as an example of application to remote sensing products. A relevant feature was the arrival of a Saharan dust intrusion from 13 to 15 July, yielding the increase of aerosol optical depth at 550 nm from 0.1 to 0.5 because of changes in the vertical distribution of aerosols, with a transport layer located between 1.5 and 4 km. An accurate knowledge of these aerosol features will be relevant in future implementation of atmospheric correction code of the airborne and satellite hyperspectral imagery.

Citation: Estellés, V., F. Molero, J. L. Gómez-Amo, J. C. Fortea, R. Pedrós, M. P. Utrillas, M. Pujadas, L. Guanter, and J. A. Martínez-Lozano (2008), Characterization of the atmosphere during SEN2FLEX 2005 field campaign, *J. Geophys. Res.*, *113*, D09205, doi:10.1029/2007JD009237.

1. Introduction

[2] A precise understanding of the global carbon cycle is required to account for the effect of the emission of carbon dioxide into the atmosphere by human activity, recognized as one of the main drivers of climate change [*Houghton et al.*, 2001; *Soon et al.*, 2001]. As the interactions between vegetation and the atmosphere are fundamental to the carbon cycle, an adequate quantification of the biosphere's ability to sequester carbon from the atmosphere is mandatory [*Cao and Woodward*, 1998; *Cox et al.*, 2000]. The photosynthetic activity directly relates with this vegetation's ability to absorb atmospheric carbon dioxide, and it can be determined measuring the solar induced fluorescence emitted by vegetation [*Freedman et al.*, 2002; *Krause and Weis*, 1991]. Monitoring this parameter at global scale would greatly improve the estimates of vegetation photosynthetic activity, allowing a better description of the role of terrestrial vegetation in the global carbon cycle and its response to climate variability under the increasing pressure of human activity [*Davidson et al.*, 2003]. As currently there are no measurements of this parameter available from satellites, the Fluorescence Explorer (FLEX) project [*Stoll et al.*, 2003] was proposed to ESA in 1998, with the main aim of global remote sensing of photosynthesis through the use of Fraunhofer lines of the solar spectrum and the atmospheric oxygen absorption bands for passive monitoring of natural sunlight-induced fluorescence [*Carter et al.*, 1996]. The exploratory phase of such ESA missions usually include demonstration activities for testing the technical capabilities of the instruments that could be launched into space in future. One of these was the SEN2FLEX (Sentinel-2 and Fluorescence Experiment) campaign [*Moreno*, 2006], carried out in Barrax (Spain) in June–July 2005. The main objectives of the campaign were twofold, first detect solar induced fluorescence signals using the AirFLEX instrument over multiple agricultural and forest targets in order to verify signal suitability for observations from space as

[1]Solar Radiation Research Unit, Universitat de València, Valencia, Spain.
[2]Unidad de Contaminación Atmosférica, Departamento de Medio Ambiente, CIEMAT, Madrid, Spain.
[3]Departamento de Física de la Terra i Termodinàmica, Universitat de València, Valencia, Spain.
[4]Remote Sensing Section, GeoForschungsZentrum Potsdam, Potsdam, Germany.

0148-0227/08/2007JD009237$09.00

proposed in the FLEX Earth Observation mission, and second provide feedback to the Agency on key issues related to the definition of the ESA Sentinel-2 multispectral mission requirements [*Rast*, 2005], such as the optimal multispectral configuration for monitoring plant pigments and so derive photochemical indicators of vegetation status, which is currently being defined under the GMES (Global Monitoring for Environment and Security) initiative. This includes the simulation of Sentinel-2 products using different sensor configurations (spatial/spectral/temporal coverage) and the evaluation of product performance as a function of configuration. The above objectives required the coordinated collection of different data sets: satellite (CHRIS/Proba [*Barnsley et al.*, 2004] and MERIS [*Rast et al.*, 1999] as the main sensors), airborne (AirFlex [*Moya et al.*, 2004], INTA-AHS [*Fernandez-Renau et al.*, 2005] and CASI [*Chen et al.*, 1999]), ground-level data over agricultural and forested areas in the central Spanish region of La Mancha and atmospheric parameters. Campaign participants were from 26 different institutions in eight different countries included teams from Universities in Valencia, Albacete, Castellón, Naples, Milan, Strasbourg, London, Lisbon along with national research institutes in Spain (INTA, CEDEX, CIEMAT, ITAP, DIELMO, CSIC, INM), France (LURE, INRA), Italy (CNR), Netherlands (ITC), Germany (DLR), and Canada (ITRES).

[3] The quality of the retrieved geophysical quantities from space- or airborne-based sensors is directly related to the accuracy of the atmospheric correction algorithm [*Kaufman et al.*, 1997; *Singh and Saull*, 1988]. It is therefore important to perform a careful quantification of the atmosphere's influence in order to obtain spatially and spectrally consistent data sets. The new sensors are based on narrow channels coincident with atmospheric absorption features or hyperspectral-multiangular measurements, and the correct exploitation of the provided data needs atmospheric radiative transfer models coupled with the surface-parameter retrieval algorithms to account for atmospheric gaseous absorption features [*Nakajima et al.*, 2003; *Verhoef and Bach*, 2003]. In this paper, the characterization of the atmosphere performed during the SEN2FLEX campaign is summarized. It was undertaken by three teams: the Solar Radiation Research Unit and the Earth Physics Department of University of Valencia, together with the Atmospheric Pollution Unit of CIEMAT, with the aim of obtaining an adequate characterization of those atmospheric constituents necessary to implement a suitable atmospheric correction of aircraft and satellite imagery. Four types of measurements were done simultaneously to the aircraft and satellite overpasses: (1) spectroradiometric and Sun photometric measurements, (2) free soundings, (3) aerosol physicochemical characterization at ground level, and (4) LIDAR aerosol vertical profiles. Measurements performed at ground level by Sun photometric and radiometric systems allow us to characterize the properties of the atmospheric components in the whole column. The temporal evolution of aerosol, water and ozone content, and main properties of aerosols (phase function, single scattering albedo, refractive index, size distributions, vertical distribution…) have been intensively recorded for an accurate atmospheric characterization. LIDAR measurements determine the vertical profile of the aerosol extinction coefficient, allowing a characterization of the diurnal evolution of the aerosols vertical structure. Changes in this structure can have some importance for the detailed atmospheric corrections of hyperspectral/multiangular data due to its influence in the adjacency effect [*Minomura et al.*, 2001]. In the first part of the paper, we briefly describe the campaigns and the different instruments used in the atmospheric characterization. In the second part, the main features of the experimental results are throughout discussed and compared with model predictions or satellite data, when available. Also, cross checking among the different instruments providing similar by-products, as CIMEL and MICROTOPS Sun photometers and radiosounding with respect to columnar water vapor, or Sun photometer and LIDAR with Aerosol Optical Depth (AOD), will be analyzed. We have also take advantage of this field campaign database to deeply discuss an interesting Saharan dust outbreak episode occurred in one of the intensive missions. Finally, we comment the foreseen analysis and data processing focusing on atmospheric correction improvement, with an example of application for validation of CASI products and an estimation of the effects of the real measured atmosphere in the airborne or satellite retrievals.

2. Measurement Campaigns and Instrumentation

2.1. SEN2FLEX Campaign

[4] The SEN2FLEX campaign was carried out at an agricultural test site located in Barrax (39°3′44″N, 2°6′10″W), close to the town of Albacete, in the La Mancha region, a plateau 700 m above sea level. Its core site is a 25 km^2 area within which numerous crops are grown, on both irrigated (approximately 35%) and dry land (65%), alongside fields of bare soil. An additional advantage of the Barrax site is its flat topography which simplifies the preprocessing required to correct for geometric and radiometric distortions (needed for the analysis of multiangular observations).

[5] The climatic and geomorphologic properties of the Barrax area, as well as the permanent facilities for surface flux and meteorological data, have been previously described [*Moreno et al.*, 2001]. The main activities in this area started when it was selected as a test site for the EFEDA experiment (European International Project on Climatic and Hydrological Interactions between Vegetation, Atmosphere and Land Surface, Field Experiment in Desertification Threatened Areas) in 1991 [*Bolle et al.*, 1993]. The Barrax area was also selected by ESA as a test site for the preparatory activities for the Land Surface Processes and Interactions Mission (LSPIM), as well as for SPECTRA (Surface Processes and Ecosystems Changes Through Response Analysis), two Earth Explorer candidate Core Missions.

[6] Two intensive field measurement campaigns were carried out between 1 and 3 June 2005 (Mission 1) and between 11 and 15 July 2005 (Mission 2). Measurements included soil (GER and ASD ground radiometers), vegetation (covering leaf area index, fCover, leaf Chlorophyll a + b, leaf water content, leaf biomass and relevant information on the phenology of each type of crop) and atmospheric characterization (radiosoundings, ground-based aerosol LIDAR, high-spectral-resolution direct/global surface radiance measurements and Sun photometer measurements)

[*Moreno*, 2006]. Although the whole campaign data has been analyzed and archived, in this work we have centered our emphasis on the results from the second mission because of the more interesting atmospheric features.

2.2. Instrumentation

2.2.1. CIMEL Sun Photometer

[7] The CIMEL CE318-NE Sun photometer allows the measurement of direct solar and sky diffuse radiance in 9 channels in the UV, VIS and NIR ranges (340, 380, 440, 500, 670, 870, 940, 1020, 1610 nm). Bandwidth is about 2 nm (at 340 nm), 4 nm (at 380 nm), 10 nm (440 to 1020 nm) and 40 nm (1610 nm). Direct Sun measurements are performed at least every 15 min and sky diffuse measurements at least once every hour. Aerosol optical depth, Ångström wavelength exponent α (a parameter that informs about the size of the optically active aerosols) and columnar water vapor are derived from the direct Sun measurements. A complete description of the employed methodology is given by *Estellés et al.* [2006]. Other aerosol properties can be retrieved from the radiance measurements if an inversion code is applied. In our case, the SKYRAD.PACK code version 4.2 have been used [*Nakajima et al.*, 1983]. It allow us to retrieve the aerosol size distribution, complex refractive index, single scattering albedo, asymmetry parameter, and other secondary derived columnar properties as effective radius, columnar aerosol mass, volume and surface. More details on the application of the code to these data are given by *Estellés* [2006].

2.2.2. MICROTOPS II Sun Photometer

[8] This handheld instrument provides a measure of the amount of ozone and water vapor in the whole atmospheric column by means of direct solar irradiance measurements at three channels for ozone (305, 312 and 320 nm) and a channel for water vapor (936 nm) respectively, plus a measure of direct solar irradiance at 1020 nm, used for deriving the AOD at this channel for assisting the estimation of the water vapor. During the campaign, direct measurements are performed at least every 15 min.

2.2.3. LIDAR System

[9] The LIDAR system is a mobile equipment based on a Nd:YAG laser source (Continuum model NY82−20) operating at the 2nd harmonic (532 nm). The laser energy was 20 mJ/pulse, expanded five times and operated vertically because of safety reasons. Other instrument characteristics have been described elsewhere [*Molero and Jaque*, 1999]. The detection window, selectable by a pulse generator that switch the detector gain, was chosen with 1 μs delay respect to the laser fire and 20 μs duration, which produced return signals from 250 to 6000 m above ground level, (agl hereafter). These signals were range-corrected and spatially averaged to improve the signal-to-noise ratio, obtaining a range resolution of 6 m. Each signal corresponds to a temporal average of 1200 laser pulses (1 min). Finally, the signals were inverted to derive vertically resolved aerosol extinction coefficient and integrated to provide aerosol optical depth (AOD) at 532 nm. The aerosol extinction-to-backscatter ratio was assumed constant and equal to 40 (continental aerosols). The Rayleigh extinction coefficient was calculated from standard atmosphere profile using the *Bodhaine et al.* [1999] revision of the theory. The measurements protocol consists on a vertical characterization with data acquisition interval of 15 min. In the 2-h interval around the satellites (ENVISAT and MODIS) and aircrafts (CessnaC208(DLR) and CASA212(INTA)) overpass time, the interval was reduced to 5 min.

2.2.4. Sounding Equipment

[10] The vertical distribution of atmospheric water vapor, temperature, pressure, wind speed and wind direction were measured using meteorological helium filled balloons equipped with Vaisala RS80 radiosondes. These radiosondes are equipped with pressure, temperature and humidity sensors integrated in a light box, completed with the GPS sensor. All parameters are measured at regular intervals and transmitted to the surface by radio signals. The equipment was completed with a ground station AIR Inc. TS-2AR Receiver s/n 259 for the signal reception. The altitude of the sonde can be computed using the hydrostatic equation, which is a function of the pressure. Relative humidity is directly measured by capacitive thin film sensor with reliable response even at low temperatures and after exposure to condensation. Wind speed and direction are not directly measured but computed by the ground equipment from the GPS information about the sonde position. Two balloons were released each day, one in the early morning before the mixing layer develops and another at the satellite overpass time, in order to characterize the precise water vapor profile in the lower layers, which change rapidly during the day because of solar heating.

2.2.5. Ground-Level Aerosol Characterization

[11] The optical particle size analyzer GRIMM mod. 1108 provides particulate counts distributed in 15 channels (0.15, 0.2, 0.25, 0.325, 0.4, 0.5, 0.8, 1.0, 1.5, 2.0, 2.5, 3.75, 5, 7.5 and 10 μm) by 90° laser light scattering. The ambient air, drawn into the unit, passes through a flat laser beam, produced by a laser diode and the scattered signals are detected by a multichannel pulse height analyzer for size classification. These data, in the form of particle counts, may be converted to a volume distribution based on the particulate matter diameter or a mass distribution using hardware coded particulate density, providing values averaged every 5 min.

2.2.6. CASI-1500 Airborne Data

[12] The Compact Airborne Spectrographic Imager (CASI) is a pushbroom imaging spectrometer measuring in the visible and near-infrared (VNIR) spectral regions. In particular, CASI-1500 samples the 370−1050 nm wavelength range, under a spectral resolution up to 2.2 nm and pixel size about 3 m. The instrument operation, the radiometric calibration, and the geometric correction were on charge of Itres Research Ltd., Calgary, Canada. Data from twelve flight lines were acquired by CASI-1500 in morning (around 0800 UTC) and noon (around 1200 UTC) flights at an altitude of 2060 m above the ground level. For these flights, CASI was operated according to two different modes. One measured in 288 channels with bandwidths of 2.2 nm and field of view (FOV) equal to 23.6°, and the other measured in 144 channels with bandwidths of 4.4 nm and FOV of 39.3°.

3. Methodology

3.1. Ozone and Water Vapor Columnar Content

[13] For the columnar ozone content measurement the MICROTOPS II Sun photometer was employed, by using

the methodology described by *Morys et al.* [2001]. The ozone columnar content from TOMS instrument [*McPeters et al.*, 1998] was also downloaded from TOMS website (http://jwocky.gsfc.nasa.gov/) and compared with the daily mean value of the MICROTOPS retrievals. In several intercomparison campaigns, the MICROTOPS ozone retrievals were compared to simultaneous data series from collocated Brewer spectrophotometers, giving a relative deviation less than 2% [*Estellés et al.*, 2003].

[14] The water vapor columnar content (w) measurements were obtained with the CE318 and MICROTOPS II Sun photometers, as well as from the radiosondes. The method chosen for calculating w by means of Sun photometry is well established [*Bruegge et al.*, 1992; *Estellés et al.*, 2006] and it is currently the standard method used by AERONET [*Holben et al.*, 1998] for the CE318 instruments. For the MICROTOPS, a very similar method was applied [*Morys et al.*, 2001] with the *Halthore et al.* [1997] fit parameters. The uncertainty of the water vapor retrieval has been estimated to be around 0.15–0.20 cm, based in different intercomparisons between instruments of the same type [*Estellés et al.*, 2004a; *Sabbah et al.*, 2001].

[15] A systematic dry bias in Vaisala radiosonde humidity measurements has been reported in comparison to Raman lidar measurements [*Ferrare et al.*, 1995] and satellite water vapor retrievals [*Soden and Lanzante*, 1996]. Vaisala, the radiosonde manufacturer, determined that the source of the dry bias was contamination of the capacitive RH sensor by outgassing of the packaging materials used on the RS80 radiosondes. In order to correct this, the humidity data provided by the radiosondes have been corrected for the chemical contamination using the algorithm published by *Wang et al.* [2002] and also temperature-dependent corrected using the coefficients published by *Miloshevich et al.* [2001].

3.2. Aerosol Optical Depth and Ångström Exponent

[16] The AOD can be retrieved from the measurements of the atmospheric extinction of direct solar radiation by applying the Bouguer-Lambert-Beer law, cancelling the contribution of the gaseous components in the instrumental channels. In the CIMEL channels the only components that show nonnegligible absorption are ozone (Chappuis band), water vapor and NO_2. Thus the total atmospheric optical depth can be expressed as:

$$\tau_T(\lambda) = \tau_R(\lambda) + \tau_{O_3}(\lambda) + \tau_{NO_2}(\lambda) + \tau_a(\lambda) + \tau_w(\lambda) \qquad (1)$$

where $\tau_R(\lambda)$ is the optical depth due to molecular scattering (Rayleigh scattering), and τ_{O3} (λ), τ_w (λ) and τ_{NO2} (λ) are the optical depths due to ozone, water vapor and NO_2 absorption respectively. For the absorption due to water vapor and NO_2 we took a standard atmosphere, corrected for site height. The correction due to ozone is necessary since the optical depth of ozone in the Chappuis band represents, on average, 8% of the total atmospheric optical depth. This value depends on the wavelength, being only 4% at 500 nm [*Pedrós et al.*, 2003].

[17] To determine the total atmospheric optical depth with the Bougher-Lambert-Beer law, the optical mass was obtained from the empirical expression proposed by *Kasten and Young* [1989]. The contribution due to Rayleigh scattering was calculated following *Bodhaine et al.* [1999]. The water optical depth was retrieved through the expression given by SMARTS model [*Gueymard*, 2001] applying the measured columnar water vapor values from the MICROTOPS, as in the case of the ozone optical depth.

[18] The error propagation was applied to obtain the AOD uncertainty [*Russell et al.*, 1993]. This uncertainty in AOD is mainly determined by the uncertainty of the direct spectral calibration and modulated by the value of the optical mass, with maximum values when the optical mass values are minima. The direct component calibration is performed by transfer from other Langley plot calibrated instruments [*Estellés et al.*, 2007] and an improved in situ Langley plot method (SKYIL) based on the SKYRAD calibration method for PREDE instruments [*Campanelli et al.*, 2007]. The diffuse component is calibrated by darkroom measurements of a NIST traceable radiance integrating sphere in a 6 months basis.

[19] The Ångström fitting parameters (α and β) were obtained using a log-log fit of the experimental AOD values versus the wavelength following the Ångström's law [*Angstrom*, 1929].

$$\tau(\lambda) = \beta\lambda^{-\alpha} \qquad (2)$$

In this equation, β coincides with the AOD at 1 μm, and α is related to the size distribution of aerosols. Roughly, for values of α lower than 1, the coarser particles dominate the size distribution. For higher than 1, the finer particles has a stronger contribution to the total aerosol burden.

3.3. Aerosol Size Distribution

[20] The aerosol size distribution (in terms of volume) must be determined by using inversion algorithms. Those of *King et al.* [1978], *King* [1982], *Nakajima et al.* [1983], and *Nakajima et al.* [1996] (called SKYRAD) have been applied to this database, in spite of only presenting the results from the SKYRAD model. The King algorithm can be run with only spectral AOD, but the derived distributions are valid only for narrower radius interval than the distributions derived from SKYRAD package. The reason is that SKYRAD employs also the sky radiance distribution in the almucantar plane; therefore the information content is higher. The King method is occasionally useful, mainly when the sky is not completely cloudless and the sky radiance is not available for inversion. In those cases, King retrievals represent a backup solution. In our case the sky was clear so the Nakajima code is clearly preferable most of times.

[21] The SKYRAD algorithm retrieves the size distribution from direct solar F and diffuse sky E spectral radiation measurements. When measured at ground level, these components for a monochromatic radiation are given by:

$$F = F_0 \exp[-m_0\tau] \qquad (3)$$

$$E(\Theta) = Fm_0[\omega\tau P(\Theta) + q(\Theta)] \qquad (4)$$

where ω, τ, $P(\Theta)$ are the single scattering albedo, optical depth and phase function (in terms of the scattering angle) for the complete atmospheric column. In these equations,

m_0 is the optical mass and q(Θ) a multiscattering term. Except m_0 all the rest magnitudes have a spectral character but the λ subindex has been eliminated to avoid excessive notation.

[22] *Nakajima et al.* [1983] developed an optimized radiative transfer code for a plane-parallel atmosphere called the Reduced Multiple scattering program (REDM). This radiative transfer code constitutes the nucleus of the SKYRAD family of inversion algorithms. In this case version 4.2 was chosen. It is a freely available algorithm that can be downloaded at the OpenCLASTR website (http://www.ccsr.u-tokyo.ac.jp/~clastr/). It was initially developed for PREDE POM sky-Sun photometers, although it has been recently adapted for CIMEL instruments. A CIMEL compatible version is being prepared for its distribution on the OpenCLASTR (http://www.ccsr.u-tokyo.ac.jp/~clastr/) together with the CIMEL adapted package for the application of the SKYRAD improved in situ Langley plot method (SKYIL) described by *Campanelli et al.* [2007].

[23] To work with the diffuse component *E*, the ratio R(Θ) is defined:

$$R(\Theta) = \frac{E(\Theta)}{Fm_0} = \omega\tau P(\Theta) + q(\Theta) = \beta(\Theta) + q(\Theta) \qquad (5)$$

where $\beta(\Theta)$ is the total dispersion coefficient, that includes single molecular and aerosol scattering. The method consist of iteratively eliminate the multiple scattering term q(Θ) from the data R(Θ) to isolate the coefficient $\beta(\Theta)$. As in the previous equations (3) and (4), except m_0 all the rest magnitudes have a spectral character but the λ subindex has been eliminated for simplicity. In every step the algorithm retrieves the volume distribution V(r) by inversion of $\beta(\Theta)$ and $\tau_a(\lambda)$. This distribution is used as input for the radiative transfer code in order to recalculate in turn R'(Θ), which is compared with the experimental data to evaluate the RMS difference ε(R). The process is repeated until ε(R) is less than 10%. If this maximum deviation between synthetic and experimental data is not reached, the process is stopped and the solution is discarded.

[24] Once the volume distribution functions are retrieved, they can be modeled by a bilognormal or trilognormal function, given by:

$$\frac{dV}{d\ln r} = \sum_{i=1}^{n} \frac{V_i}{\sqrt{2\pi}\ln\sigma_I} \exp\left[-\frac{1}{2}\left(\frac{\ln(r/r_{Mi})}{\ln\sigma_i}\right)^2\right] \qquad (6)$$

where r_{Mi} is the modal radius for the mode *i* (being n = 2 or 3 depending on the case), ln σ_i is the standard deviation of the mode, and V_i is the modal volume.

3.4. Aerosol Vertical Profile

[25] The LIDAR signals were inverted to derive vertically resolved aerosol extinction coefficient profiles using the equation published by *Sasano and Nakane* [1984] based on the Klett inversion method [*Klett*, 1981]. The aerosol extinction-to-backscatter ratio was assumed to be constant and equal to 40 (continental aerosols). The Rayleigh extinction coefficient was calculated from standard atmosphere profile using the *Bodhaine et al.* [1999] revision. The profiles were integrated between ground-level and 6 km agl, after ascertain that no aerosol burden was present over that height by visually inspecting each LIDAR profile, to provide AOD at 532 nm. As mentioned before, the LIDAR signal started at r > 200 m instead of at ground level (r = 0) since the dependency on the inverse of the squared range makes the signal dynamic range too wide if the complete signal is considered. In order to compare the AOD obtained by the integration of the extinction coefficient profiles with those provided by the CE318, that take into account the whole column, we assumed a well-mixed layer between the surface and the height where the LIDAR signal starts and assigned this layer a constant extinction coefficient value equal to the value obtained for 200 m. This value was added between the ground and the start of the signal, as suggested by *Ferguson and Stephens* [1983].

3.5. Retrieval of Atmospheric Parameters From CASI-1500 Data

[26] As in the case of other airborne instruments covering the VNIR, the atmospheric state is characterized from CASI data in terms of the total aerosol content, parameterized by the AOD at 550 nm (ADO550 hereafter), and w at the time of image acquisition. AOD must be derived in the first place, in order to properly account for the effects of aerosol scattering on the NIR wavelengths to be considered for w retrieval. A full description of the methodology for the retrieval of AOD and w from CASI data is reported by *Guanter et al.* [2007]. Only a brief overview is presented here.

[27] The general procedure for the estimation of atmospheric parameters from remote sensing data consists in the inversion of at-sensor radiance measurements against a given surface-atmosphere model constrained by parameters defining the acquisition scenario and the atmospheric state. Atmospheric radiative transfer calculations are performed here by a modified version of the widely known MODTRAN4 radiative transfer code [*Berk et al.*, 1998].

3.5.1. Retrieval of AOD

[28] The technique for the AOD550 retrieval was designed to work over rural areas and assumes that the aerosol loading is not changing within some kilometers, which is the typical size of the imaged area. A representative AOD value is derived from a set of reference spectra with the maximum spectral contrast, from green vegetation to bare soil. This spectral contrast in the surface, while assuming a constant atmosphere for all the reference pixels, enables the decoupling between atmospheric and surface contributions. AOD is derived by inversion of reference pixels through the minimization of a merit function comparing the real reference spectra with simulated ones. For this simulation, reflectance is built as a linear combination of two end-members, typical vegetation and soil reflectance spectra. The abundances of vegetation and soil are retrieved as by-products from the inversion process, as well as the sought AOD.

[29] Because the aerosol loading is described by the AOD550 and the rural aerosol model, which is fixed in advance, important errors may occur in those cases in which real aerosols are not properly described by the rural model, such as dust intrusions or air masses containing maritime aerosols. However, previous analysis shown that there is not

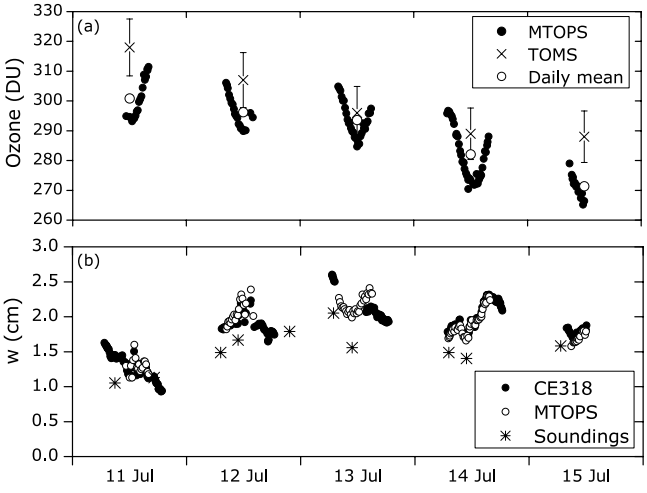

Figure 1. Temporal evolution of the (a) ozone and (b) water vapor columnar contents during the second mission (11–15 July 2006). The MTOPS ozone uncertainty is estimated to be 2%, while the EP/TOMS uncertainty is around 3%. The MTOPS and CE318 water vapor columnar content have an estimated uncertainty of 0.15 cm.

enough spectral information in CASI data over land targets for the reliable estimation of the aerosol model in addition to AOD550. The inability to derive information about the aerosol type is then assumed to be intrinsic limitation of the method.

3.5.2. Retrieval of w

[30] Retrieval of w is based on the evaluation of the water vapor absorption feature centered at 940 nm. A band-fitting technique was preferred to band-ratio ones for w ones [*Carrere and Conel*, 1993; *Schlapfer et al.*, 1998] in order to minimize the noise intrinsic to CASI data, which is relatively high because of the fine spectral and spatial resolution acquisition mode.

[31] The method was designed so that the maximum information from the CASI high spectral sampling could be extracted. w is derived from the inversion of the at-sensor radiance around 940 nm on a per-pixel basis. An estimation of surface reflectance around those wavelengths is necessary for the inversion of w. However, surface reflectance around the 940 nm region cannot be known until w is estimated. To solve this interdependence, two different spectral regions are considered. The first, from 860 to 890 nm, is assumed to be free from water vapor absorption, apart from a residual continuum absorption. The second one, from 890 to 930 nm, is affected by the left wing of the 940 nm water vapor absorption. It is not extended to 940 nm to avoid errors coming from a bad evaluation of the vegetation liquid water absorption feature, centered about 950 nm, whose effects are noticeable in 940 nm. Reflectance at the water vapor free region is derived by using a default w value of 1.5 cm. It is then extended to the second region by extrapolation, assuming that reflectance in the 860–930 nm spectral window is linear with wavelength for land targets. The w value obtained by this procedure can be refined by a second iteration, which updates the default w value with the output from the first iteration. A w map showing the spatial distribution of water vapor is obtained as a final result.

4. Results

[32] All atmospheric correction codes require considerable amount of atmospheric data for their calculations and the key problem is the availability and accuracy of these data. A common solution is the input of some generalized, averaged values for each parameter (models assimilated in the code). The effects of the atmosphere on radiative transfer can be divided in two contributions: from gases, mainly ozone and water vapor, and from aerosols. The gaseous contribution is rather well defined and can be derived accurately once the state of the atmosphere is known. The parameters required include temperature, pressure and molecular densities at different altitudes extracted from meteorological data. The aerosol contribution is more problematic because the exact calculations require both the local particle density and particle distribution, which in general are not available because of the lack of suitable measuring stations. In this work we have provided a filtered and analyzed database as accurate as possible for the application to remote sensing applications. We have included an instance of an application to this field campaign in section 4.

4.1. Gaseous Components

[33] Figure 1a shows the evolution of the ozone column for the 5 days of the Mission 2 campaign and compares with the daily mean values provided by EP/TOMS [*McPeters et al.*, 1998]. The ozone column was retrieved by the MICROTOPS II Sun photometer with an estimated uncertainty of 2% [*Estellés et al.*, 2003]. As it can be seen in Figure 1a, the daily evolution has a minimum value near noon with maximum values at sunrise and sunset. Also, a steady decrease is observed along the campaign, well reproduced by the TOMS data. The coefficient of determination (COD hereafter) provided by linear regression of the Microtops data to the TOMS data is 0.76, indicating a moderate degree of correlation between both data sets. In terms of RMSD (relative deviation between both data sets), the comparison gives a value of 5.4 DU (4%). The TOMS data is always higher than the MICROTOPS, as it has been previously reported after a comparison with a 30 ground-based station network [*McPeters and Labow*, 1996]. Also, increased Mie scattering resulting from the presence of tropospheric aerosols has been observed to significantly affect the radiances measured by TOMS. [*Torres et al.*, 1998], which might explain the better agreement found on 13 and 14 July, when elevated dust-rich layer where present, in comparison with 11 and 15 July, with well-mixed boundary layer, as it will be shown later.

[34] Figure 1b shows the evolution of the columnar water vapor measured by means of MICROTOPS II (black circles), CIMEL (open circles) and, also, the value obtained by integrating the radiosonde relative humidity values (stars), previously transformed to absolute humidity. Different daily evolutions were found during the 5 days. The highest columnar water vapor values were measured on 13 July at early morning and seems due to the presence of high clouds. A fairly good agreement is found between the

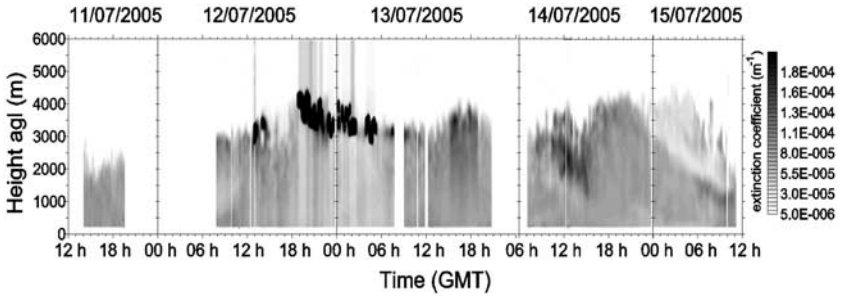

Figure 2. Atmospheric aerosols structure obtained by interpolating the extinction coefficient profiles provided by the CIEMAT LIDAR during the 5 days of the SEN2FLEX 2005. The gaps are due to technical problems in the data acquisition. The black dots on the mornings of 12 and 13 July are caused by the intense backscattering signal produced by clouds. Dust-rich elevated layers are observed on the afternoon of 13 July (1400–1900 UTC) and the morning of 14 July (1000–1600 UTC).

MICROTOPS and the CE318 Sun photometers (COD = 0.93, with a RMSD of 0.09 cm for 65 data values), while the radiosonde seems to underestimate the total value (COD = 0.35, RMSD = 0.31 cm). Radiosonde relative humidity measurements are known to be unreliable at cold temperatures and temperature-dependent, time lag and radiation correction factors need to be applied [*Miloshevich et al.*, 2001]. In this case, the relative humidity profiles were corrected for the chemical contamination and also temperature-dependent corrected which increased the columnar water vapor between 2 and 5%. As that was not enough to reach the MICROTOPS and CE318 values, further corrections seems necessary. In previous intercomparisons between Sun photometric and radiosounding derived values, the conclusions were equivalent [*Martinez-Lozano et al.*, 2007].

4.2. Aerosols

4.2.1. Aerosol Extinction Coefficient

[35] The aerosol extinction coefficient vertical profiles evolution can be represented by interpolating all the LIDAR measurements. Figure 2 shows a gray-coded plot of this evolution from 11 to 15 July. The horizontal axis represents time and the vertical axis is height above ground level. The gray scale represents the extinction coefficient, expressed as m^{-1}. The black spots on the evening and night of 12 July and morning of 13 July are clouds. The analysis of the LIDAR results shows a clear evidence of the arrival of a aerosol rich layer at high levels that affected the vertical distribution of aerosols on 13–15 July. The vertical structure found on 14 July shows a high aerosol load layer located between 1.5 and 4 km and probably decoupled from surface. Such structure is due to the arrival of dust-rich elevated layers from the Sahara. During the night of 14 July and the morning of 15 July, the aerosol load in the boundary layer decreased slowly, leaving a residual layer above it, as it can be seen in the right-most part of Figure 2.

[36] In order to confirm the above explanation, the HYSPLIT model [*Draxler and Rolph*, 2003] was used to compute the air mass back trajectories arriving at the site at different times. The so calculated trajectories give a hint about the path followed by the air mass and therefore, the type of particles that it could carry. For each day, HYSPLIT 5 day back trajectories have been obtained with the available vertical velocity model at three different heights over ground: 500 m (within the boundary layer), 1500 m (near the transition between the boundary layer and the free atmosphere) and 3000 m (in the free atmosphere). Figure 3 shows the output results of the model, indicating the different nature of the air masses for the July period. For 11 July, all vertical levels show a northern (European) origin. However, the situation changes along the campaign. On 14 July, the air masses show a clear passage over the Sahara region and surroundings at high altitude, and on 15 July the middle altitude back trajectory can clearly carry desert dust from Argelia.

[37] As the back trajectories do not fully support the above explanation, a more precise predictor of dust load, the Dust Regional Atmospheric Model (DREAM) [*Nickovic et al.*, 2001] has been employed. It is specifically designed to simulate and/or predict the atmospheric cycle of mineral dust aerosol. Its predictions at 0000 UTC for the campaign days are presented in Figure 4. In these predictions, 11 to 13 July showed no particular dust influence, but on 14 and 15 July, some dust was clearly present over Southeastern Spain, affecting the vertical distribution of aerosols as it was shown in Figure 3. Regarding the position of the measuring site, Barrax, at the outermost part of the Saharan dust plume, that could explain the different results obtained taken into account the reduced accuracy of the predictions on these areas. Anyhow, the results seem consistent and the increase on turbidity was related to an intrusion of dusty air from northern Africa, and the aerosol probably was partially formed by mineral particles, mainly on 14 and 15 July.

4.2.2. Aerosol Optical Depth (AOD)

[38] The evolution of the AOD at 532 nm (AOD532 hereafter) is shown in Figure 5. Two data sets are represented: (1) AOD interpolated to 532 nm using the Ångström exponent estimated from direct solar measurements provided by the CE318 Sun photometer (black circles) and (2) AOD obtained by integrating the aerosol extinction profiles provided by the LIDAR, at 532 nm (open circles).

[39] Several features may be noticed in Figure 5: First, the data shows a good agreement on 14 July, and slightly worse on 12 and 13 July. although better than expected taken into account that the inversion procedure of the LIDAR signal include several assumptions that need to be properly checked, and also because the integration of the extinction coefficient profile increases the noise of the data because of the low SNR of the far-range signal. Despite of these, the

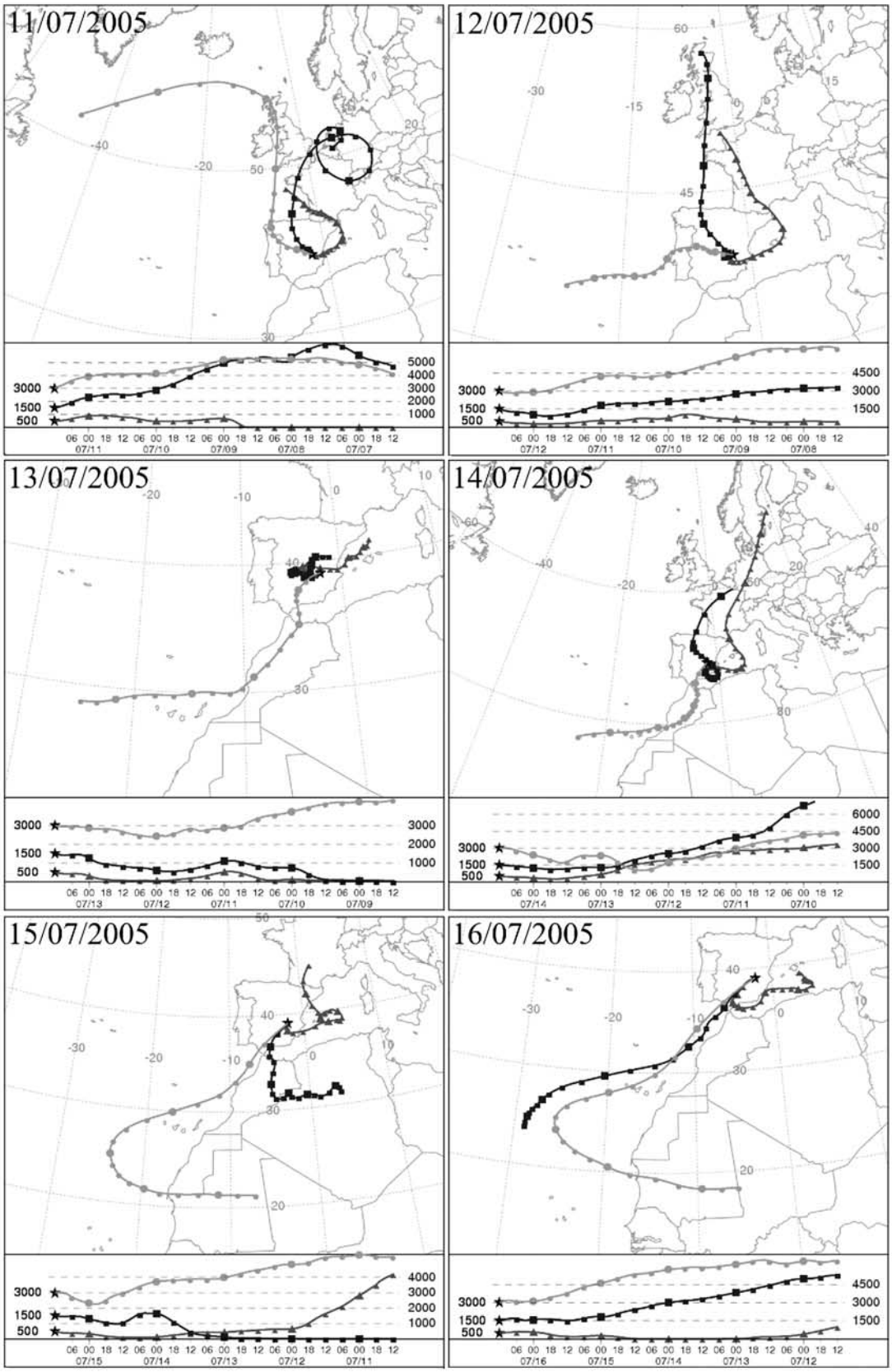

Figure 3. Five-day back trajectories for Mission 2 days, ending at Barrax (39.05°N, 2.10°W) at 1200 UTC at three different altitudes (500 m a.g.l. (squares), 1500 m a.g.l. (triangles) and 3000 m a.g.l. (circles)), computed with NOAA HYSPLIT4 model using FNL meteorological data and model vertical velocity calculation method.

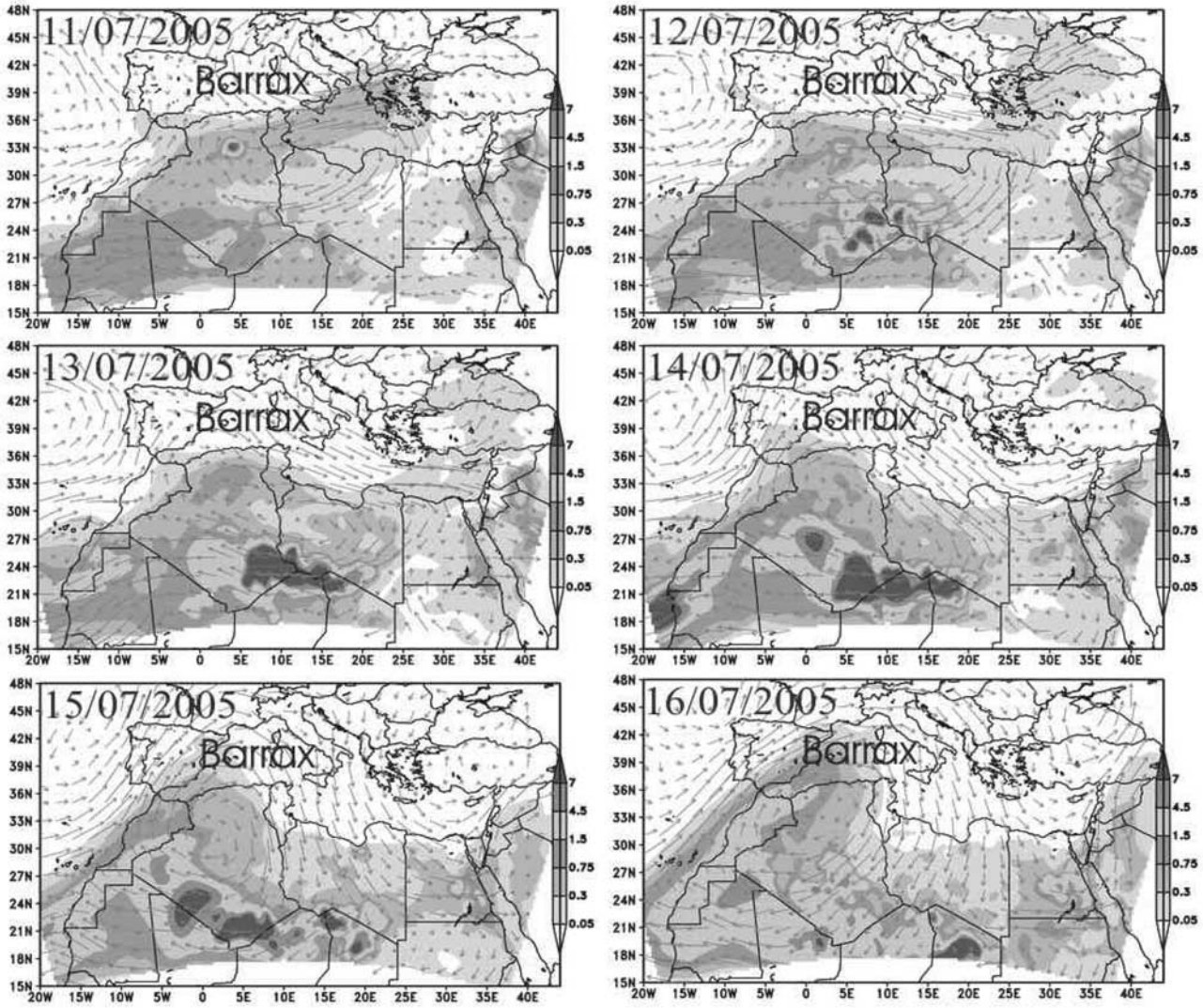

Figure 4. Zero-hour forecast of dust loading (g m^{-2}) and 3000 m wind from the BSC/DREAM model for 11–16 July 2005 at 1200 UTC.

AOD532 values provided by the LIDAR seem reasonable. Second, on 11 July, when the AOD532 is very low, the measurements clearly disagree. This can be explained on the basis of the limitation of the LIDAR to measure low optical depth [*Kunz and Deleeuw*, 1993] due to the large errors caused by the limited maximum dynamic range of the system, as compared with the inverse value of the extinction coefficient. The opposite situation occurs on 15 July, when the CE318 measured a AOD532 over 0.3 while the LIDAR provides values around 0.2. During 14 July, the Saharan outbreak clearly has reached the site, increasing steadily the AOD532 at 532 nm from 0.15 to 0.45 during the morning but only the outermost part of the air mass overflown the area, as it was shown in Figure 4, and during the evening and night the LIDAR data indicate a significant decrease of the desert dust load (see Figure 2). The Sun photometer data also suffers a less steeped decrease. A linear regression between both data sets provided a COD of 0.26, indicating the bad correlation between them. When the above mentioned disagreements are masked in the fit, COD increases to 0.43, still a rather low correlation that indicates the problems implied by calculating the AOD532 from the LIDAR vertical profiles.

4.2.3. Aerosol Volume Distributions

[40] The GRIMM size distributions are presented in Figure 6 for 11 and 14 July, as well as the distributions

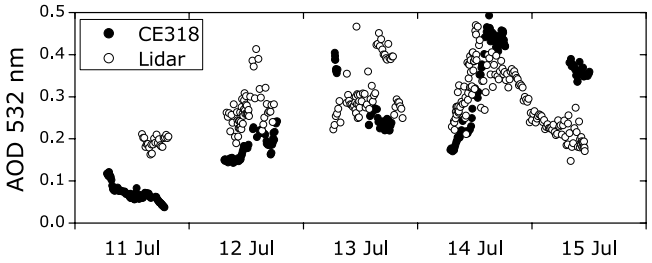

Figure 5. AOD at 532 nm provided by the CE318 and that obtained by integrating the extinction coefficient profiles provided by the LIDAR system, for Mission 2.

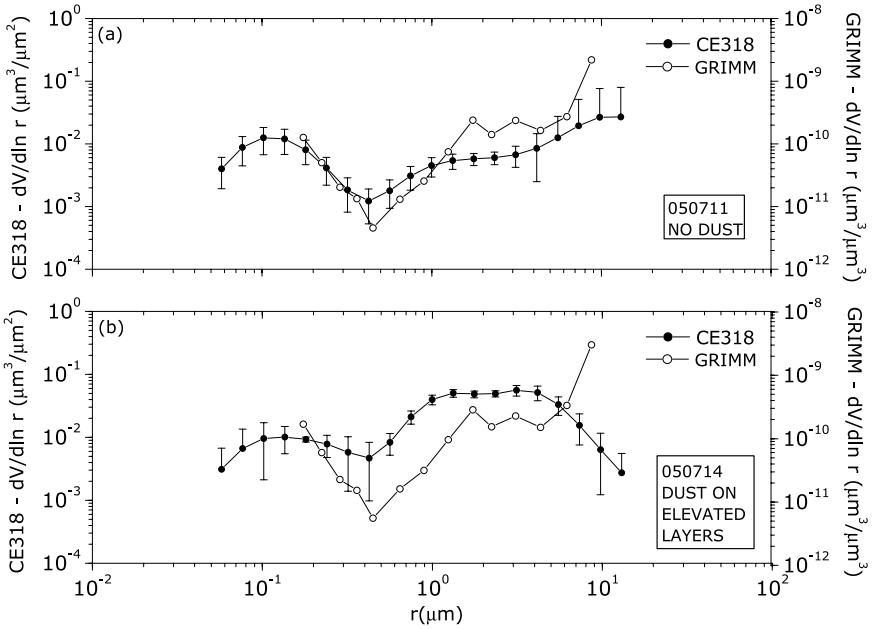

Figure 6. Comparison of the ground-level size distribution provided by the GRIMM 1108 and the columnar size distribution obtained by inverting the direct solar measurements provided by the CE318 for (a) 11 July and (b) 14 July 2005.

retrieved with the CE318 Sun photometer, for comparison. For the Sun photometer, the SKYRAD inversion code has been applied to the sky radiance data in the 0.05–15 μm radius interval. In Figure 6 we can see how both GRIMM and CE318 distributions are very similar for 11 July, but they differ for 14 July. Taken into account that the CIMEL distributions are representative of the whole atmospheric column, meanwhile the GRIMM measurements are only representative of the lower layers, it indicates that once the CE318 distributions were detecting the arrival of elevated dust layers, the desert dust was not reaching the surface as it was not detected by the in situ instruments, supporting the explanation of a dust-rich elevated layer decoupled from surface indicated by analyzing the LIDAR vertical profiles.

[41] In Figure 7 the mean daily volume distributions are plotted for the Mission 2 period, as retrieved by the SKYRAD algorithm. In general, the distributions show a trimodal shape. The accumulation mode would be composed by fine particles like soots from local or remote European pollution but also from agricultural or far biomass fires (anthropogenic origin) or by very small particles from other species. The two other coarser modes would be mainly related to mineral species, from local or remote origin (local continental soils or remote dust), but also to oceanic-marine species (mainly salts) from further origin (Atlantic or Mediterranean).

[42] In Figure 7, the fine mode increases its height from 11 to 13 July, decreasing after 13 July, in spite of a continuous but slight modal radius increase. As no chemical analysis of the aerosol has been made, no definitive conclusions can be draw for this behavior, although we can try to explain this trend based in the greater influence of increasing fractions of fine mineral particles that would affect the modal radius, at the time that the remote sources of anthropogenic pollution increase their influence on 11 and 12 July and gradually disappear when the dominant air masses change their origin to Southern regions (13 July on).

[43] Both coarser modes show the modal radius to decrease. On turn, the first coarse mode steadily increases its height, but the second coarse mode increases from 11 to 13 July, decreasing afterward. A hypothesis is that the remote dust particles start to dominate the rural background, getting more peaked coarse modes over the flatter and lower local background. The coarser particles from remote origin would have not arrived over the site, instead of local particles of bigger size, very dependent on meteorological conditions. In any case it must be remembered that the

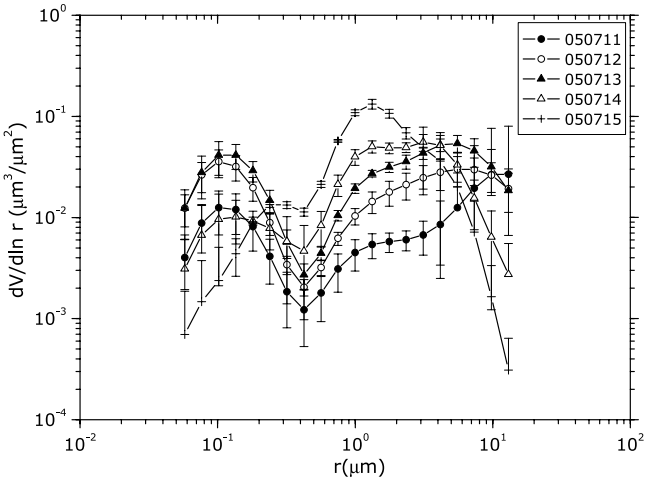

Figure 7. Daily mean aerosol volume distributions retrieved by the SKYRAD algorithm for Mission 2 days. The parameters obtained after fitting these distributions to trimodal lognormal functions are shown in Table 1.

Table 1. Parameters Obtained When Fitting the Daily Volume Distributions in Figure 7 to Trimodal Lognormal Functions[a]

Date	V_f, $\mu m^3/\mu m$	σ_f	r_f, μm	V_{c1}, $\mu m^3/\mu m$	σ_{c1}	r_{c1}, μm	V_{c2}, $\mu m^3/\mu m$	σ_{c2}	r_{c2}, μm
11 Jul 2005	0.015	1.59	0.11	0.014	2.53	2.26	0.034	1.67	12
12 Jul 2005	0.041	1.57	0.11	0.028	2.08	1.99	0.045	1.97	7.4
13 Jul 2005	0.051	1.60	0.12	0.027	1.61	1.36	0.084	1.87	5.2
14 Jul 2005	0.018	1.99	0.15	0.043	1.49	1.23	0.065	1.61	3.5
15 Jul 2005	0.0016	1.59	0.27	0.14	1.51	1.28	0.039	1.51	3.5

[a]V, σ and r parameters refer to modal volume, width and radius. Subscripts f, c1 and c2 refer to the fine, medium coarse and upper coarse modes.

extremes of the wings in the distributions suffer from a much higher uncertainty.

[44] This distribution evolution is clearly seen if we inspect the parameters from the lognormal functions that were fitted to the distribution curves (a trimodal lognormal function). For reference, these fit parameter sets are presented in Table 1, for Mission 2 days.

4.2.4. Other Sizing Parameters

[45] There are some other simple but useful parameters that can be derived from the size distributions in order to be applied, for instance, in radiative models. We have derived the effective radius, the volume concentration and the mass concentration.

[46] The most important parameter for radiative transfer modelization in the atmosphere is the effective radius, and represents the ratio between the total volume and surface of the aerosols in the atmospheric column [*van de Hulst*, 1957].

[47] The effective radius has been presented in Figure 8a for the whole period including Missions 1 and 2 (i.e., June and July). The data gaps are due to instrumental fails (mainly data server shutdowns) and cloud contaminated data or not convergent retrievals. It is interesting to note that the effective radius was maximum at the Mission 2, but it was also high during Mission 1 (1 and 2 June). In Mission 2, the radius increased from the background values (around 0.4 μm) to the total maximum of the campaign (around 0.7 μm).

[48] The mass concentration in the atmospheric column has been presented in Figure 8b. It has been computed assuming a given particle density of 1.9 g/m^3 [*D'Almeida et al.*, 1991] as an average value for the whole set of data and applying it to an integral over the size distribution range. The evolution shows a maximum mass concentration for the Mission 2 period, with a constant increasing trend from the start of the mission (11 July) to its end (15 July). High values were also reported for Mission 1 period, although they were not so high as in July. Assuming a given particle density we only pretend to describe qualitatively the trends of mass concentration with the arrival of Saharan air mass. If we take into account the particles from Saharan dust episode, the value assumed for the particle density should be changed when the intrusion arrives because these particles would increase average particle density. In this case the observed increasing trend would be more evident.

4.2.5. Refractive Index

[49] The refractive index is also computed with the SKYRAD algorithm by a minimization technique based on the deviation between the synthetic sky radiance distribution and the experimental measurements in the almucantar plane, by a two dimensional sweep algorithm. This algorithm was not included in SKYRAD version 2. Although an uncertainty statement for the refractive index retrieval is not yet published, there is some work in progress (T. Nakajima, personal communication, 2007). In any case, the uncertainty of the imaginary part of the refractive index is very high mainly when the AOD is low; it would explain the high daily variability, although the trends are consistent.

[50] In Figure 9, the real (n) and imaginary (k) parts of the refractive index at 500 nm are presented. In both missions, n shows an increasing trend, starting from background values and reaching maximum values at the end of each campaign. This behavior is much more evident in July. In general, the n values are representative of continental particles (around 1.45) but they consistently increase when desert dust is expected to be present, up to 1.48 in our case. For comparison, the authors [*Estellés et al.*, 2007] found a mean annual value below 1.40 in Burjassot (Valencia, Spain) a coastal site around 150 km northeast, due to the effect of maritime particles immersed in a humid ambient. *Dubovik et al.* [2002] found values up to 1.55–1.56 in regions more directly influenced by desert aerosols (Persian Gulf and Arabia Saudi); other sites (Cape Verde) showed intermediate values (1.48 ± 0.05) more similar to our results.

[51] On the other hand, k also showed a steady decrease along both missions. This parameter is related to the absorption properties of the aerosol components. Maritime aerosols would show negligible values (negligible absorption); soot particles would show maximum absorption. Mineral dust would show intermediate values. Again, in

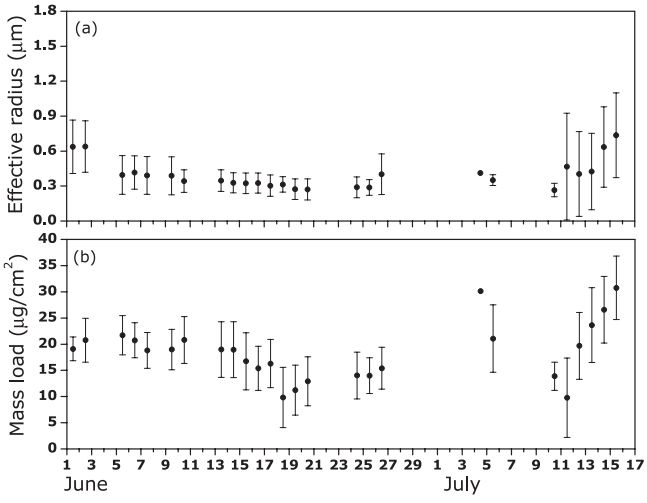

Figure 8. Evolution of (a) effective radius and (b) total aerosol mass load in the atmospheric column during the whole SEN2FLEX campaign, including Missions 1 and 2.

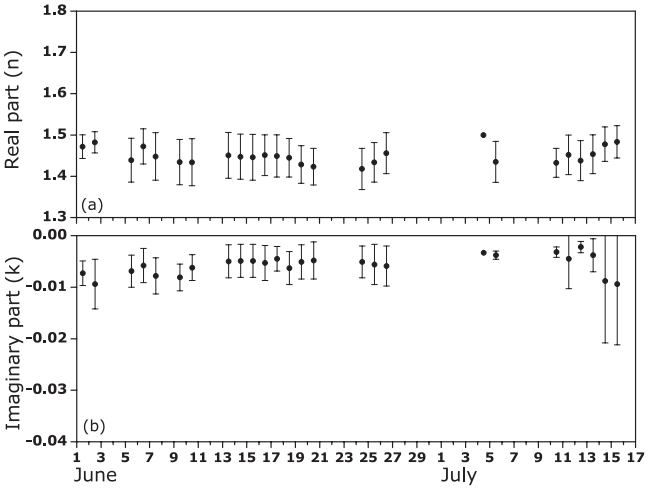

Figure 9. Evolution of (a) real and (b) imaginary part of the aerosol refractive index during the whole SEN2FLEX campaign, including Missions 1 and 2.

comparison to *Estellés et al.* [2007] results in Burjassot, our retrieved values of k are somewhat lower, pointing out less absorbent aerosols. The result is consistent when taking into account that the Burjassot site receives contributions from the sea but also suffers the strong urban influence of Valencia metropolitan area, characterized by more absorbent aerosols. As a remote clean reference, the Bahrain (Persian Gulf) site [*Dubovik et al.*, 2002] shows lower k for mineral dust; therefore, in general our measurements are coherent with a continental type aerosol as background (mineral + anthropogenic aerosols) [*Pedrós et al.*, 2003] with an increasing burden of mineral particles during the southern air mass arrivals.

4.2.6. Single Scattering Albedo

[52] The single scattering albedo (SSA or ω_0) is a key parameter related to the absorption properties of the particles (and therefore linked to the imaginary part of the refractive index) and is defined as the ratio between the extinction due to scattering and the total extinction. Therefore, the closer the SSA to 1, the less absorbent the aerosol is. As k, its uncertainty is high. No uncertainty estimation have already been published for the SKYRAD version 4.2., although a current comparison with AERONET products at Gosan (Korea) in the last UNEP/ABC/EAREX project has given a RMS difference between both SSA products of about 0.05 (K. Aoki, personal communication, 2007).

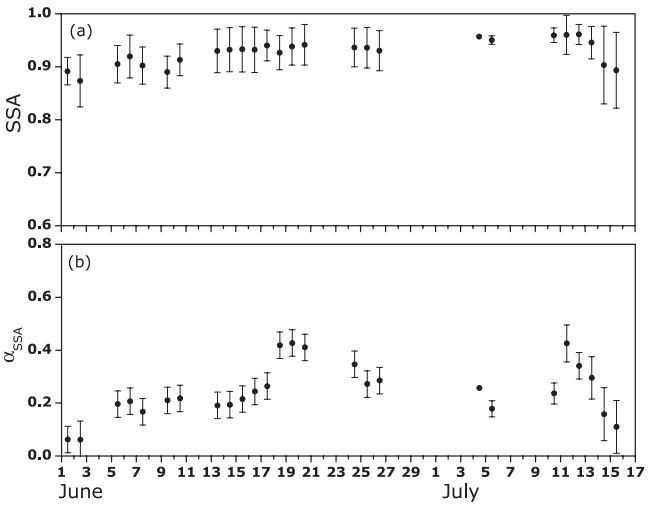

Figure 10. Evolution of (a) single scattering albedo (SSA) at 500 nm and (b) its wavelength exponent (α_{SSA}) during the whole SEN2FLEX campaign, including Missions 1 and 2.

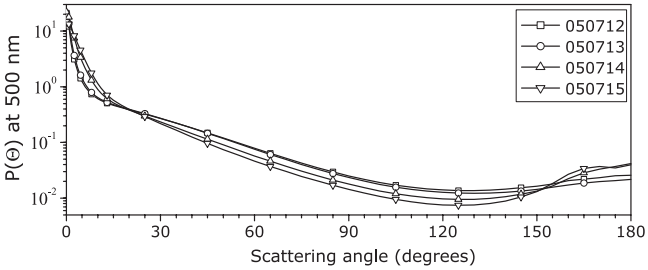

Figure 11. Aerosol phase function at 500 nm for 11–14 July 2005 (Mission 2). Note the differences in aureole and backscattering regions.

[53] In Figure 10a the evolution of the SSA at 500 nm has been plotted. A slight increasing trend can be identified along the whole measuring period. A possible explanation to this behavior could be related to the slow temporal increase of nonabsorbent components (for example salts) in the columnar aerosol total burden, although there are no auxiliary measurements for verifying this hypothesis. In any case, from 13 to 15 July we detected the expected change, with decreasing SSA through the second mission, pointing out the higher absorption of these particles, as predicted before by k. Lower SSA than total period mean were also retrieved during the first mission in June, also affected by Saharan air masses.

[54] *Coen et al.* [2004] proposed a method for identifying Saharan dust outbreaks at the Jungfraujoch consisting on analyzing the wavelength dependence of the SSA. If fine particles dominate, the SSA diminishes with λ. If large particles dominate, the SSA increases or is constant with λ [*Dubovik et al.*, 2002]. As the SSA correspond to the scattering part of the extinction coefficient, both absorption and scattering terms can be modeled also with a power law function, as in the case of the total extinction, modeled by

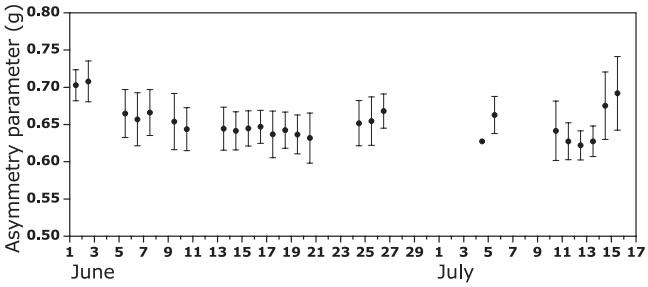

Figure 12. Evolution of the asymmetry parameter at 500 nm during the whole SEN2FLEX campaign, including Missions 1 and 2.

the Ångström law in equation (2). Therefore the dependence of the SSA on λ can be fitted to:

$$\omega_0(\lambda) = \beta_{SSA}\lambda^{-\alpha_{SSA}} \quad (7)$$

Coen et al. [2004] proposed to define the dust events by the sign of the α_{SSA} exponent. We have computed α_{SSA} by the equation (7). In Figure 10b, the evolution of the so retrieved SSA exponent is given. As can be seen, the α_{SSA} reached minimum values during both missions, in spite of being always positive. For Mission 2, the situation completely changed from maximum to minimum values.

[55] In spite of the decreasing trend of α_{SSA}, no negatives values were reached. Therefore, the criteria proposed by *Coen et al.* [2004] cannot be applied. It is actually sensible to find no negative values in our case: Jungfraujoch is a very high site (3580 m a.s.l.) over the continental boundary layer and therefore under pristine conditions, i.e., very low aerosol burdens. The occasional dust outbreaks, when detected from this site, must completely affect the columnar properties; in our case, as we are immersed within the boundary layer, the dust will only partially affect the columnar properties and therefore no pure properties will be reached. In other words, the criteria proposed by Coen *et al.* cannot be applied, although the spectral dependence trends will help for recognizing dust entrances.

4.2.7. Aerosol Phase Function and Asymmetry Parameter

[56] The aerosol phase function P_a represents the angular distribution of energy as scattered by the particle. It can be modeled for an isolate particle by the Mie theory [*van de Hulst*, 1957], but for retrieving the phase function for the columnar aerosol, the retrieved size distribution must be taken also into account within the inversion procedure, and the molecules phase function must be canceled from the sky radiance measurements.

[57] In Figure 11 the phase function for 11 and 15 July is plotted. In this case, the difference between dust and no-dust situations is reflected in the aureole region (brighter and wider aureoles) and in the backscattering region, where the coarse particles make the radiance grow at 500 nm between 160° and 180° of scattering angles.

[58] The phase function is a parameter linked to the size and shape of the particles, although it is a complex function of wavelength, scattering angle and refractive index. For the radiative transfer codes, the asymmetry parameter g is usually employed for characterizing the aerosol scattering properties. It is computed from the actual phase function as the second term of a polynomial Legendre serie and can be understood as an angular average of this function, getting therefore angle-independent. The asymmetry parameter depends mainly on the size parameter ($2\pi r/\lambda$) which takes into account the relationship between the particle size and the wavelength of the incident radiation. If we used only a wavelength of 500 nm the asymmetry parameter can be used also as a size indicator of the particles, getting close to 1 when the energy is completely scattered forward (coarse particles) and 0 when is symmetrically scattered backward and forward (molecules). The retrieved g is showed in Figure 12 for the complete database.

[59] As expected, the maximum values of g were retrieved on Mission 1 and 2 days; for Mission 2, a steady increasing trend was found again, depicting a situation where the aerosol size distribution was getting more and more dominated by coarse dust particles due to the entrance of southern air masses.

[60] On the basis of our analysis, we can therefore conclude that both intensive missions suffered from dust outbreaks that undoubtedly affected the measurements performed with airborne and satellite sensors; moreover, the dust was distributed in elevated layers, so the signal would be differently disturbed if measured in airborne or satellite platforms, even in different flights at different heights. Therefore, an accurate analysis of the atmospheric situation must be always taken into account for an adequate processing of the resulting campaign data.

4.2.8. Comparison With a Maritime-Polluted Nearby Site

[61] The aerosol horizontal and vertical distribution is very sensitive to spatial and temporal changes, because of the immense variety of sources and aerosol types, hygroscopic properties, ambient conditions, and aging. At a given site and time, the instantaneous columnar properties will be defined by a superposition of local and remote terms. Local sources usually are characterized by strong fluctuations, in relation to local meteorology. Remote contributions imprint a more relaxed spatial distribution, as in the case of desert dust outbreaks.

[62] A final test was performed with the SEN2FLEX photometric data, for checking the spatial variation of aerosol optical and radiative properties. For this purpose, we compared the Barrax database with that simultaneously obtained at Burjassot (Valencia) with a second CE318 Sun photometer, also operated by the Solar Radiation Research Unit. Burjassot is a site immersed in the metropolitan Valencia area, populated by 1,400,000 inhabitants. The site is therefore very affected by urban and industrial pollution, and also under the influence of desert outbreaks and of maritime (Mediterranean) ambient conditions.

[63] The intercomparison for the intensive mission days is shown in Figure 13a for the AOD at 500 nm and Figure 13b for the Ångström exponent. The other properties are not shown for briefness, but give equivalent conclusions. In both missions, a similar trend is detected in both sites; this main trend is related to large-scale aerosol layers. Superimposed, smaller-scale changes are distinguished. In general, aerosol burden in Burjassot used to be slightly higher, because of extra pollution contribution. This contribution can be also found in α value, generally higher than Barrax, pointing out a size distribution dominated by finer particles, probably of anthropogenic origin. For example, on 11 July a short-term increase of AOD500 is detected in Burjassot; this is usually related to breeze effects [*Estellés et al.*, 2004b] and it is not found in Barrax.

[64] In relation to the dust episode detected in Mission 2, and comparing the evolution with Figure 4 where the predicted spatial dust distribution was shown, some features can be recognized. First, the main trends are simultaneously followed by both sites. Second, the dust effects are first detected in Barrax: the decrease of α starts a few hours before, and the usually lower AOD increases rapidly over Burjassot values. A few hours later, AOD and α measured at Burjassot follow the same trend. This is coherent with model predictions, because the dust layer seems to arrive at

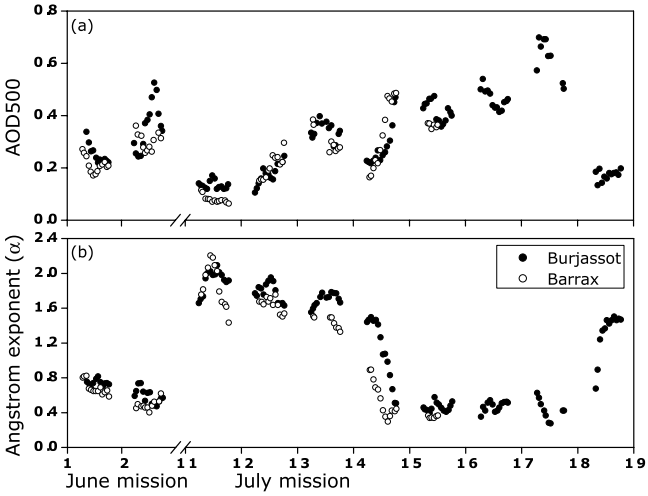

Figure 13. Evolution of (a) AOD500 and (b) α exponent during the Mission 1 and 2 days, as simultaneously measured by two CE318 instruments at two sites: Barrax and Burjassot. Burjassot data have been presented for full dust outbreak (up to 19 July).

both sites southwesterly; therefore it would affect Barrax in first place. Third, the trend is stabilized at the end of 14 July, when both sites remain approximately at the same isoconcentration line. Moreover, on 14 July the winds bring the air masses directly from continental north Africa; on 15 July, the wind speed has increased and seems to bring the dust from the Canary islands region.

[65] In Figure 13 we have included data up to 19 July 2005. Although the data collection was ended at Barrax on 15 July, the data from Burjassot was not discontinued and shows further evolution of the dust outbreak that increased its strength in the region. The α exponent was stabilized for 3 days, in spite of an increase of the total aerosol burden as seen in Figure 13a. After the outbreak, the usual background levels were recovered for both aerosol burden and size.

5. Application to Remote Sensing Products

[66] As we have mentioned before, an accurate analysis of the atmospheric state and properties during the intensive field campaigns was very useful for the correction of remote sensing data. An illustrative example comes from the validation of CASI atmospheric products. Figure 14 displays the comparison between CASI and the ground-based instrument CIMEL CE318 retrievals of AOD550 (Figure 14a) and w (Figure 14b). Points correspond to measurements performed in 5 different days, 1, 2, and 3 June (Mission 1) and 13 and 14 July (Mission 2), at the time of the aircraft flight, in the morning and noon. CASI was operated in two different modes, one measuring 288 channels (open circles) and other measuring 144 channels (crossed circles). CE318 values are represented as filled circles and their error bars correspond to the standard deviation in the ground measurements in a 2 h window centered at the time of CASI acquisition, while the uncertainty estimated for each single measurement is 0.02. Because of instrumental failures of CE318 on 13 July at the CASI acquisition time, an

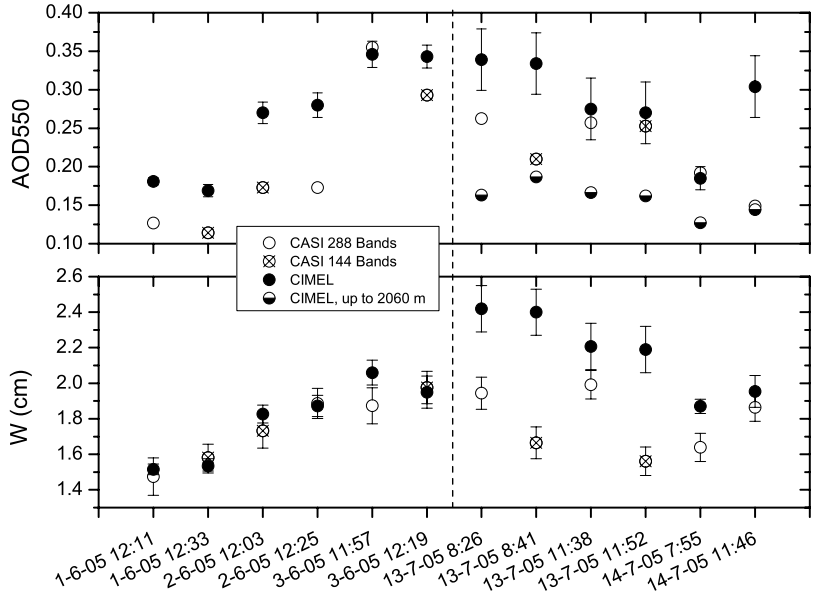

Figure 14. Compared retrievals of (a) AOD550 and (b) w for CE318 and CASI instruments. Points correspond to measurements performed in 5 different days, 1, 2, and 3 June (Mission 1) and 13 and 14 July (Mission 2), at the time of the aircraft flight. CASI was operated in two different modes, one measured in 288 channels (open circles) and other in 144 channels (crossed circles). Half-solid circles correspond to the percentage of the CIMEL AOD550 values equal to the estimated contribution of aerosols up to 2060 m calculated by integrating the LIDAR extinction profiles. The error bars for CE318 show the standard deviation of data over a 2 h window around the CASI acquisition. CASI error bars for w refer to the standard deviation of the w retrievals in the 1.2×1.2 km^2 area around the location of the CE318 instrument. No error budget is calculated for the AOD retrievals from CASI.

interpolation between the available data, also considering the trend observed at Burjassot (Valencia), was performed, which increased the uncertainty of the measurement. Abrupt changes in illumination due to clouds also affect the quality of the measurements on 13 July. No error budget is calculated for the AOD retrievals from CASI. The LIDAR extinction profiles, only available for Mission 2, have been integrated up to 2060 m, the aircraft flight altitude agl, in order to estimate the amount of aerosols below and above the aircraft. The corresponding percentage of the CIMEL AOD550 values below the aircraft are shown as half-solid circles in Figure 14a. Concerning AOD loading retrieval, it can be concluded that temporal variations can in general be reproduced by CASI retrievals. Similar temporal trends are found in CE318 and CASI-derived values, especially if data from 13 July are discarded. A systematic underestimation of CASI retrievals with respect to ground-based measurements can also be noted.

[67] There are some particular conditions under which important discrepancies between remote sensing and ground-based measurements are expected. One major error source in aerosol retrieval from airborne sensors is the vertical distribution of aerosols, as this information is not used in the processing of remote sensing data. The estimated AOD value is always related to the aerosol vertical profile and type which are used in the inversion procedure. The larger the deviation of the real aerosol profile from the one selected in the atmospheric model is, the larger the error becomes. This effect is maximized in the case of dust intrusions at high altitudes, especially over the mixing layer. In those situations, a considerable proportion of aerosols is located above the sensor. This causes that most of the path radiance, which is the radiation scattered by the atmosphere into the sensor line of sight, is generated above the aircraft, so it cannot be measured by CASI. Since the path radiance is directly correlated to aerosol scattering, and it is a maximum at the shortest wavelengths, where the surface is the darkest, it is the variable providing most of the information for AOD estimation. The path radiance generated in the layers above the aircraft because of abnormal aerosol layers cannot be modeled by the standard aerosol profiles implemented in MODTRAN. As a result, important underestimations of the retrieved aerosol loading are found when compared to ground-based measurements, which do measure the entire column. Such situation is observed on 14 July, at noon, when the episode of Saharan dust intrusion was clearly detected, as it has been discussed in previous sections. The aerosol layers entered into the Barrax site with a height from 1.5 to 4 km agl, which is higher than the 2060 m aircraft flight height. As a result, the AOD550 value obtained from airborne measurements (0.144) underestimates the one provided by the Sun photometer (0.304). But when the contribution of the aerosols below the aircraft is applied, CIMEL value reduces to 0.149, showing a good agreement between both instruments. However, such deviation should not affect the subsequent retrieval of surface reflectance from CASI data, as the estimated AOD is consistent with the aerosol parameters set in the radiative transfer code. It must be noted that the error in AOD would be much smaller in the case of satellite observations, as all the path radiance generated along the atmospheric column would be measured by the sensor. Remotely sensed and ground-based AOD retrievals would then be comparable.

[68] Water vapor retrievals are plotted in Figure 14b. Again, CE318 error bars are the standard deviation of the w calculated from all the ground measurements taken in a 2 h window centered at the time of CASI acquisition. The uncertainty associated to each single measurement is 0.15 cm [*Estellés et al.*, 2006]. CASI error bars refer to the standard deviation of the w retrievals in the 1.2×1.2 km^2 area around the location of the CE318 instrument. The dependence on the water vapor vertical profile is not as important as it is for particulate matter, because the experimental vertical profile provided by radiosounding conform better with the radiative transfer code standard profile. In any case, better agreement is found in Mission 1 (1–3 July) than in Mission 2 (13 and 14 July) probably related with the arrival of the Saharan outbreak, that affects the aerosol but also the water vapor vertical profiles, as the dust-rich layer also carried high columnar water content and several clouds on the morning of 13 July. This also seems to affect the 144 bands mode producing worse estimations of w than the 288 band mode in the morning and noon of 13 July. However, the sensitivity of the calculus to the different acquisition modes, with different band number, spectral resolution, field of view and optical path might be larger than the effects of the vertical distribution on the final product.

6. Conclusions

[69] In this work we have analyzed an intensive atmospheric characterization during the SEN2FLEX-ESA field campaign, with the aim of improving the atmospheric correction on the satellite and airborne products to be retrieved. The set of experimental data obtained allows a suitable characterization of the atmosphere in terms of the required inputs for atmospheric correction codes. Regarding the interpretation and improvement of satellite retrievals, several potentially interesting situations have been documented. For instance, the situation on 14 July 2005 showed an elevated layer with an aerosol load consisting in large-size aerosols from the Sahara. The analysis of the data, regarding both experimental and modeling (back trajectories (HYSPLIT) and 3-D tracer model (DREAM)) results, have shown evidences of the arrival of a Saharan dust intrusion from 13 to 15 July, the most significant atmospheric phenomenon of the whole campaign. During this event, the AOD at 550 nm increased from 0.1 to 0.5 and the vertical distribution of aerosols presented a transport layer located between 1.5 and 4 km, with higher aerosol loading in the transport layer than in the mixing layer. These different aerosol distributions provide a very useful data set that has been applied to test the atmospheric correction of hyperspectral/multiangle aircraft imagery. An example of the usefulness of aerosol vertical profiles in the interpretation of airborne-based AOD retrievals has also been presented. The underestimation in CASI-derived AOD at 550 nm when compared to ground Sun photometric measurements during an episode of Saharan dust intrusion was justified by the discrepancy between the aerosol vertical profile introduced into the radiative transfer code and the experimental one provided by the ground LIDAR technique. However, such discrepancy should not affect the

retrieval of surface reflectance from CASI data, as the estimated AOD is consistent with the aerosol parameters set in the radiative transfer code. The correction of the CIMEL value, to take into account only the contribution of aerosols located below the aircraft flight height improved the agreement between both instruments but further investigations seems necessary to fully understand the effects involved.

[70] **Acknowledgments.** The authors would like to thank the members of all the groups participating in SEN2FLEX for their collaboration, especially J. Moreno, the coordinator of the project. Víctor Estellés was granted by the Spanish Ministry of Science and Technology, reference FP2000-5488, dependent on DEPRUVISE project (REN 2000-0903-C03). The authors gratefully acknowledge the NOAA Air Resources Laboratory (ARL) for the provision of the HYSPLIT transport and dispersion model (READY website http://www.arl.noaa.gov/ready.html) used in this publication and the Spanish Meteorological Institute (INM) for providing the meteorological instrumentation used in the campaigns.

References

Angstrom, A. (1929), On the atmospheric transmission of Sun radiation and on dust in the air, *Geogr. Ann.*, *11*, 156–166, doi:10.2307/519399.

Barnsley, M. J., et al. (2004), The PROBA/CHRIS mission: A low-cost smallsat for hyperspectral multiangle observations of the Earth surface and atmosphere, *IEEE Trans. Geosci. Remote Sens.*, *42*(7), 1512–1520, doi:10.1109/TGRS.2004.827260.

Berk, A., et al. (1998), MODTRAN4 version 3 revision 1 user's manual, technical report, Air Force Res. Lab., Hanscom Air Force Base, Mass.

Bodhaine, B. A., et al. (1999), On Rayleigh optical depth calculations, *J. Atmos. Oceanic Technol.*, *16*(11), 1854–1861, doi:10.1175/1520-0426(1999)016<1854:ORODC>2.0.CO;2.

Bolle, H. J., et al. (1993), Efeda—European Field Experiment in a desertification-threatened area, *Ann. Geophys.*, *11*(2–3), 173–189.

Bruegge, C. J., et al. (1992), Water-vapor column abundance retrievals during FIFE, *J. Geophys. Res.*, *97*(D17), 18,759–18,768.

Campanelli, M., et al. (2007), Application of the SKYRAD improved Langley plot method for the in situ calibration of CIMEL Sun-sky photometers, *Appl. Opt.*, *46*(14), 2688–2702, doi:10.1364/AO.46.002688.

Cao, M. K., and F. I. Woodward (1998), Dynamic responses of terrestrial ecosystem carbon cycling to global climate change, *Nature*, *393*(6682), 249–252, doi:10.1038/30460.

Carrere, V., and J. E. Conel (1993), Recovery of atmospheric water vapor total column abundance from imaging spectrometer data around 940 nm—Sensitivity analysis and application to airborne visible/infrared imaging spectrometer (AVIRIS) data, *Remote Sens. Environ.*, *44*(2–3), 179–204, doi:10.1016/0034-4257(93)90015-P.

Carter, G. A., et al. (1996), Detection of solar-excited chlorophyll a fluorescence and leaf photosynthetic capacity using a Fraunhofer Line Radiometer, *Remote Sens. Environ.*, *55*(1), 89–92, doi:10.1016/0034-4257(95)00192-1.

Chen, J. M., et al. (1999), Compact Airborne Spectrographic Imager (CASI) used for mapping biophysical parameters of boreal forests, *J. Geophys. Res.*, *104*(D22), 27,945–27,958, doi:10.1029/1999JD900098.

Coen, M. C., et al. (2004), Saharan dust events at the Jungfraujoch: Detection by wavelength dependence of the single scattering albedo and first climatology analysis, *Atmos. Chem. Phys.*, *4*, 2465–2480.

Cox, P. M., et al. (2000), Acceleration of global warming due to carbon-cycle feedbacks in a coupled climate model, *Nature*, *408*(6809), 184–187, doi:10.1038/35041539.

D'Almeida, G. A., et al. (1991), *Atmospheric Aerosols: Global Climatology and Radiative Characteristics*, A. Deepak, Hampton, Va.

Davidson, M., et al. (2003), Mapping photosynthesis from space—A new vegetation-fluorescence technique, *ESA Bull.*, *116*, 34–37.

Draxler, R. R., and G. D. Rolph (2003), HYSPLIT (Hybrid Single-Particle Lagrangian Integrated Trajectory) model, Air Resour. Lab., NOAA, Silver Spring, Md. (http://www.arl.noaa.gov/ready/hysplit4.html).

Dubovik, O., et al. (2002), Variability of absorption and optical properties of key aerosol types observed in worldwide locations, *J. Atmos. Sci.*, *59*(3), 590–608, doi:10.1175/1520-0469(2002)059<0590:VOAAOP>2.0.CO;2.

Estellés, V. (2006), Caracterización de los aerosoles atmosféricos en Valencia mediante fotometría solar, Ph.D. thesis, Univ. de València, València, Spain.

Estellés, V., et al. (2003), Analysis of performance of a Microtops II Sunphotometer for ozone retrieval in comparison with a Brewer spectrophotometer in Sodankylä, Finland, paper presented at IX WMO/GAW Brewer Users Group Meeting, World Meteorol. Organ., Huelva, Spain.

Estellés, V., et al. (2004a), Aerosol related parameters intercomparison of CIMEL sunphotometers in the frame of the VELETA 2002 field campaign, *Opt. Pura Apl.*, *3*, 3289–3297.

Estellés, V., et al. (2004b), Study of a frequent transitory aerosol plume effect related to meteorological conditions in a Mediterranean coastal site, *Int. J. Aerosol Sci.*, *XX*, 591–592, spec. issue.

Estellés, V., et al. (2006), Intercomparison of spectroradiometers and Sun photometers for the determination of the aerosol optical depth during the VELETA-2002 field campaign, *J. Geophys. Res.*, *111*, D17207, doi:10.1029/2005JD006047.

Estellés, V., J. A. Martinez-Lozano, M. P. Utrillas, and M. Campanelli (2007), Columnar aerosol properties in Valencia (Spain) by ground-based Sun photometry, *J. Geophys. Res.*, *112*, D11201, doi:10.1029/2006JD008167.

Ferguson, J. A., and D. H. Stephens (1983), Algorithm for inverting lidar returns, *Appl. Opt.*, *22*(23), 3673–3675.

Fernandez-Renau, A., et al. (2005), The INTA AHS system, *Proc. SPIE Int. Soc. Opt. Eng.*, *5978*, 471–478.

Ferrare, R. A., et al. (1995), A comparison of water-vapor measurements made by Raman lidar and radiosondes, *J. Atmos. Oceanic Technol.*, *12*(6), 1177–1195, doi:10.1175/1520-0426(1995)012<1177:ACOWVM>2.0.CO;2.

Freedman, A., et al. (2002), Remote sensing of solar-excited plant fluorescence as a measure of photosynthetic rate, *Photosynthetica*, *40*(1), 127–132, doi:10.1023/A:1020131332107.

Guanter, L., et al. (2007), Spectral calibration and atmospheric correction of ultra-fine spectral and spatial resolution remote sensing data. Application to CASI-1500 data, *Remote Sens. Environ.*, *109*(1), 54–65, doi:10.1016/j.rse.2006.12.005.

Gueymard, C. A. (2001), Parameterized transmittance model for direct beam and circumsolar spectral irradiance, *Sol. Energy*, *71*(5), 325–346, doi:10.1016/S0038-092X(01)00054-8.

Halthore, R. N., et al. (1997), Sun photometric measurements of atmospheric water vapor column abundance in the 940-nm band, *J. Geophys. Res.*, *102*(D2), 4343–4352, doi:10.1029/96JD03247.

Holben, B. N., et al. (1998), AERONET—A federated instrument network and data archive for aerosol characterization, *Remote Sens. Environ.*, *66*(1), 1–16, doi:10.1016/S0034-4257(98)00031-5.

Houghton, J. T., et al. (2001), *Climate Change 2001: The Scientific Basis—Contribution of Working Group I to the Third Assessment Report of the Intergovernmental Panel on Climate Change*, 892 pp., Cambridge Univ. Press, New York.

Kasten, F., and A. T. Young (1989), Revised optical air mass tables and approximation formula, *Appl. Opt.*, *28*(22), 4735–4738.

Kaufman, Y. J., et al. (1997), Passive remote sensing of tropospheric aerosol and atmospheric correction for the aerosol effect, *J. Geophys. Res.*, *102*(D14), 16,815–16,830, doi:10.1029/97JD01496.

King, M. D. (1982), Sensitivity of constrained linear inversions to the selection of the Lagrange multiplier, *J. Atmos. Sci.*, *39*(6), 1356–1369, doi:10.1175/1520-0469(1982)039<1356:SOCLIT>2.0.CO;2.

King, M. D., et al. (1978), Aerosol size distributions obtained by inversion of spectral optical depth measurements, *J. Atmos. Sci.*, *35*(11), 2153–2167, doi:10.1175/1520-0469(1978)035<2153:ASDOBI>2.0.CO;2.

Klett, J. D. (1981), Stable analytical inversion solution for processing lidar returns, *Appl. Opt.*, *20*(2), 211–220.

Krause, G. H., and E. Weis (1991), Chlorophyll fluorescence and photosynthesis—The basics, *Annu. Rev. Plant Physiol.*, *42*, 313–349, doi:10.1146/annurev.pp.42.060191.001525.

Kunz, G. J., and G. Deleeuw (1993), Inversion of lidar signals with the slope method, *Appl. Opt.*, *32*(18), 3249–3256.

Martinez-Lozano, J. A., et al. (2007), Atmospheric components determination from ground-level measurements during the Spectra Barax Campaigns (SPARC) field campaigns, *IEEE Trans. Geosci. Remote Sens.*, *45*(9), 2778–2793.

McPeters, R. D., and G. J. Labow (1996), An assessment of the accuracy of 14.5 years of Nimbus 7 TOMS Version 7 ozone data by comparison with the Dobson network, *Geophys. Res. Lett.*, *23*(25), 3695–3698, doi:10.1029/96GL03539.

McPeters, R. D., et al. (1998), Earth Probe Total Ozone Mapping Spectrometer (TOMS) data products user's guide, *NASA Tech. Publ., 1998-206895*.

Miloshevich, L. M., et al. (2001), Characterization and correction of relative humidity measurements from Vaisala RS80-A radiosondes at cold temperatures, *J. Atmos. Oceanic Technol.*, *18*(2), 135–156, doi:10.1175/1520-0426(2001)018<0135:CACORH>2.0.CO;2.

Minomura, M., et al. (2001), Adjacency effect in the atmospheric correction of satellite remote sensing data: Evaluation of the influence of aerosol extinction profiles, *Opt. Rev.*, *8*(2), 133–141, doi:10.1007/s10043-001-0133-2.

Molero, F., and F. Jaque (1999), The laser as a tool in environmental problems, *Opt. Mater.*, *13*(1), 167–173, doi:10.1016/S0925-3467(99)00026-9.

Moreno, J. (2006), SEN2FLEX campaign overview, paper presented at SEN2FLEX Final Workshop, Eur. Space Res. and Technol. Cent., Eur. Space Agency, Noordwijk, Netherlands, 30–31 Oct.

Moreno, J., et al. (2001), The measurement programme at Barrax, in *Proceedings of the Final Results Workshop on DAISEX*, *Eur. Space Agency Spec. Publ.*, *ESA-SP 499*, 43–52.

Morys, M., et al. (2001), Design, calibration, and performance of MICROTOPS II handheld ozone monitor and Sun photometer, *J. Geophys. Res.*, *106*(D13), 14,573–14,582, doi:10.1029/2001JD900103.

Moya, I., et al. (2004), A new instrument for passive remote sensing 1. Measurements of sunlight-induced chlorophyll fluorescence, *Remote Sens. Environ.*, *91*(2), 186–197, doi:10.1016/j.rse.2004.02.012.

Nakajima, T., et al. (1983), Retrieval of the optical-properties of aerosols from aureole and extinction data, *Appl. Opt.*, *22*(19), 2951–2959.

Nakajima, T., et al. (1996), Use of sky brightness measurements from ground for remote sensing of particulate polydispersions, *Appl. Opt.*, *35*(15), 2672–2686.

Nakajima, T. Y., et al. (2003), Efficient use of an improved radiative transfer code to simulate near-global distributions of satellite-measured radiances, *Appl. Opt.*, *42*(18), 3460–3471, doi:10.1364/AO.42.003460.

Nickovic, S., et al. (2001), A model for prediction of desert dust cycle in the atmosphere, *J. Geophys. Res.*, *106*(D16), 18,113–18,129, doi:10.1029/2000JD900794.

Pedrós, R., et al. (2003), Column-integrated aerosol optical properties from ground-based spectroradiometer measurements at Barrax (Spain) during the Digital Airborne Imaging Spectrometer Experiment (DAISEX) campaigns, *J. Geophys. Res.*, *108*(D18), 4571, doi:10.1029/2002JD003331.

Rast, M. (2005), GMES Sentinel-2 mission requirements document, MRD, 32 pp., Eur. Space Res. and Technol. Cent., Eur. Space Agency, Noordwijk, Netherlands.

Rast, M., J. L. Bezy, and S. Bruzzi (1999), The ESA Medium Resolution Imaging Spectrometer MERIS: A review of the instrument and its mission, *Int. J. Remote Sens.*, *20*(9), 1681–1702, doi:10.1080/014311699212416.

Russell, P. B., et al. (1993), Pinatubo and pre-Pinatubo optical-depth spectra: Mauna Loa measurements, comparisons, inferred particle size distributions, radiative effects, and relationship to lidar data, *J. Geophys. Res.*, *98*(D12), 22,969–22,985.

Sabbah, I., et al. (2001), Full year cycle of desert dust spectral optical thickness and precipitable water vapor over Alexandria, Egypt, *J. Geophys. Res.*, *106*(D16), 18,305–18,316, doi:10.1029/2000JD900410.

Sasano, Y., and H. Nakane (1984), Significance of the extinction backscatter ratio and the boundary-value term in the solution for the 2-component lidar equation, *Appl. Opt.*, *23*(1), 11–13.

Schlapfer, D., et al. (1998), Atmospheric precorrected differential absorption technique to retrieve columnar water vapor, *Remote Sens. Environ.*, *65*(3), 353–366, doi:10.1016/S0034-4257(98)00044-3.

Singh, S. M., and R. J. Saull (1988), The effect of atmospheric correction on the interpretation of multitemporal AVHRR-derived vegetation index dynamics, *Remote Sens. Environ.*, *25*(1), 37–51, doi:10.1016/0034-4257(88)90040-5.

Soden, B. J., and J. R. Lanzante (1996), An assessment of satellite and radiosonde climatologies of upper-tropospheric water vapor, *J. Clim.*, *9*(6), 1235–1250, doi:10.1175/1520-0442(1996)009<1235:AAOSAR>2.0.CO;2.

Soon, W., et al. (2001), Modeling climatic effects of anthropogenic carbon dioxide emissions: unknowns and uncertainties, *Clim. Res.*, *18*(3), 259–275, doi:10.3354/cr018259.

Stoll, M. P., et al. (2003), The FLEX-Fluorescence Explorer mission project: motivations and present status of preparatory activities, paper presented at Geoscience and Remote Sensing Symposium, IGARSS '03, Inst. of Electr. Eng., Florence, Italy, 21–25 July.

Torres, O., et al. (1998), Derivation of aerosol properties from satellite measurements of backscattered ultraviolet radiation: Theoretical basis, *J. Geophys. Res.*, *103*(D14), 17,099–17,110, doi:10.1029/98JD00900.

van de Hulst, H. C. (1957), *Light Scattering by Small Particles*, John Wiley, New York.

Verhoef, W., and H. Bach (2003), Remote sensing data assimilation using coupled radiative transfer models, *Phys. Chem. Earth*, *28*(1–3), 3–13.

Wang, J., et al. (2002), Corrections of humidity measurement errors from the Vaisala RS80 radiosonde—Application to TOGA COARE data, *J. Atmos. Oceanic Technol.*, *19*(7), 981–1002, doi:10.1175/1520-0426(2002)019<0981:COHMEF>2.0.CO;2.

V. Estellés, J. L. Gómez-Amo, J. A. Martínez-Lozano, R. Pedrós, and M. P. Utrillas, Solar Radiation Research Unit, Universitat de València, E-46100 Valencia, Spain. (jmartine@uv.es)

J. C. Fortea, Departamento de Física de la Terra i Termodinàmica, Universitat de València, Dr. Moliner 50, E-46100 Valencia, Spain.

L. Guanter, Remote Sensing Section, GeoForschungsZentrum Potsdam, Telegrafenberg, D-14473, Potsdam, Germany.

F. Molero and M. Pujadas, Unidad de Contaminación Atmosférica, Departamento de Medio Ambiente, CIEMAT, Avenida Complutense 22, E-28040 Madrid, Spain.